Additive Manufacturing 73 (2023) 103699

Contents lists available at ScienceDirect

Additive Manufacturing

journal homepage: www.elsevier.com/locate/addma

Research paper

Manufacturing of single-process 3D-printed piezoelectric sensors with electromagnetic protection using thermoplastic material extrusion

Tilen Košir, Janko Slavič *

University of Ljubljana, Faculty of Mechanical Engineering, Aškerčeva 6, 1000 Ljubljana, Slovenia

ARTICLE INFO

Keywords:
Single process
Piezoelectric sensor
Piezoelectric effect
Poling
Material extrusion
Additive manufacturing
Electromagnetic interference
Electromagnetic shield
Force sensor

ABSTRACT

Material extrusion with a thermoplastic polymer enables the simultaneous fabrication and poling of piezoelectric sensors; however successful implementation of electromagnetic interference (EMI) protection has yet to be achieved. This research addresses key challenges such as encapsulating the sensor in a limited space without affecting the poling process, the high resistance of the conductive filaments causing low-pass charge filtering, and the need for electrical contact with EMI-protected measurement devices.

The presented design principles enable the fabrication of a fully 3D-printed piezoelectric sensor in a single process that includes a piezoelectric sensing element, wire, and a connector interface, all EMI-shielded. Strategies such as inter-trace extrusion filling and electrode ironing are introduced to avoid electrode short circuits and electric poling issues. In addition, the 3D-printed interface allows direct connection to commercially available connectors and measurement devices.

As a force sensor, the fully 3D-printed piezoelectric sensor with full EMI shielding has an excellent signal-to-noise ratio of 27 dB and reduces noise for more than two orders of magnitude if compared to the partially shielded sensor. This research is an important step forward in fabricating and embedding piezoelectric sensors in a single process that offers a wide range of applications in fields such as structural health monitoring, robotics, and biomedical engineering, where a high degree of customization is required.

1. Introduction

Additive-manufacturing technologies combined with traditional processes can produce smart functional structures that were previously not possible [1]; e.g., to produce 3D-printed devices and electronics [2], custom biomedical applications [3] and smart structures used in structural health monitoring [4].

In recent years, additive-manufacturing techniques for the fabrication of sensory elements have attracted considerable scientific attention [5,6] as they enable the creation of complex sensor shapes and embedding them into functional smart structures during the fabrication phases [7]. Multiple 3D-printing methods can be combined in a multi-step process to produce 3D-printed sensors. Examples include a three-axis capacitive accelerometer manufactured using vat photopolymerization (VP) and wet metallization (Zega et al. 2019) [8], a fully printed, piezoresistive-based, accelerometer fabricated using VP and screen-printing techniques (Liu et al. 2021) [9], a fully 3D-printed, piezoelectric accelerometer manufactured in a multi-step process using VP and material jetting (Bernasconi et al. 2022) [10] and a self-powered tactile piezoelectric position sensor fabricated using VP presented by Chang et al. in 2023 [11].

Additive-manufacturing processes have also shown the potential to produce functional devices in a single step as demonstrated by a ready-to-use sensor co-extruded with printable piezoelectric and conductive inks (Bodkhe et al. 2018) [12], complex piezoelectric nanogenerators (PENGs) fabricated using on solvent-assisted precipitation material extrusion 3D printing (Li et al. 2022) [13], and a fully 3D-printed soft robot with capacitive electrochemical sensors, piezoresistive strain, and temperature sensors, and magnetic actuation capability using multi-material ME technique (Wang et al. in 2023) [14].

Material extrusion (ME) with thermoplastic polymer is another promising technology for the fabrication of sensor elements due to accessibility and simple application; it has already been successfully used for the fabrication of capacitive [15–17], piezoresistive [17,18], and piezoelectric [19] sensor elements. Lee and Tarbutton were among the first to present a successful trial of the ME of piezoelectric PVDF films for sensing applications in 2014 [20]. Manufacturing 3D-printed sensors in a single process were successfully demonstrated by piezoresistive and capacitive touch sensors developed by Hohimer et al. [21] in 2020, a fully 3D-printed, single-axis, piezoresistive accelerometer presented by Arh et al. in 2021 [22], self-aware 3D-printed structures

* Corresponding author.
E-mail address: janko.slavic@fs.uni-lj.si (J. Slavič).

https://doi.org/10.1016/j.addma.2023.103699
Received 13 April 2023; Received in revised form 23 June 2023; Accepted 17 July 2023
Available online 20 July 2023

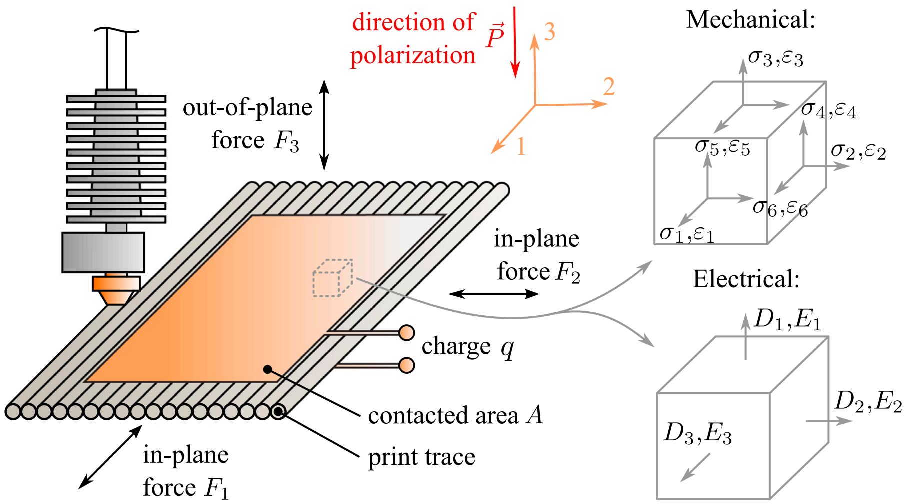

Fig. 1. Mechanical and electrical quantities in piezoelectric PVDF film fabricated by ME in a defined coordinate system [19].

with piezoresistive sensing element presented by Palmieri et al. in 2021 [23], a fully 3D-printed, piezoelectric sensor presented by Košir and Slavič in 2022 [19] and a 3D-printed soft actuator with embedded piezoresistive strain and capacitive touch sensors presented by Stano et al. in 2023. [24] In general, piezoelectric sensors using ME are more difficult to fabricate than piezoresistive sensors, but provide better sensitivity [19].

The area of ME and piezoelectric (PE) sensing is primarily concentrated on developing methods to enhance the piezoelectric sensitivity of thin piezoelectric films [19]. Homopolymer PVDF and its copolymer alternative PVDF-TrFe are the commonly used materials for ME and are commercially available in filament form. The β-phase content in the thin PVDF films plays a role in their piezoelectric performance [25,26]. To provide piezoelectric properties, the molecular dipoles must be aligned in a high electric field just below the Curie temperature [27]. Conventional methods for fabricating 3D-printed piezoelectric sensors with ME involve three main steps: film fabrication, electrode attachment, and electrical poling. Electrical poling is normally performed using contact-electrode-based poling [28] or corona poling [29]. While these methods have yielded good sensor sensitivity [25,30], the process involved multiple steps to produce 3D-printed, PE sensing elements using ME. Electric poling and ME have been successfully combined in one process in the integrated 3D-printing and corona-poling process (IPC) [31], electric poling-assisted additive manufacturing (EPAM) [32, 33], and single-process ME and electrode-based poling [19]. The single-process ME and electrode based poling method, presented by Košir and Slavič in 2022, includes all the steps required for the fabrication of PE sensors in a single process by fabricating the PE layer and the electrodes with a multi-material ME and automatically connecting the electrodes to the high-voltage terminal for electrode-based poling during fabrication.

Current research on the development of conductive 3D-printable materials for ME primarily revolves around the integration of conductive fillers, such as carbon nanotubes (CNT) [34] or CB [35], into the polymer matrix, and on post-processing techniques to enhance the conductivity of the resultant composite materials [36]. Several commercially available conductive filaments can be used for electrode deposition, including conductive polylactic acid (CPLA) [22,37], conductive thermoplastic polyurethane (CTPU) [38,39], and a conductive Electrifi filament [40], where the resistivity can vary from $3.6 \cdot 10^{-3}$ Ω cm to about 200 Ω cm and is dependant on the 3D-printing parameters [40]. Since conductive polymer materials have relatively high resistivity, electrode placement, and design must be considered because the electrode resistance combined with the capacitance of the PE film results in a low-pass filtering effect of the measured charge [41]. To establish a conductive interface between the 3D-printed conductive paths and the electrical components, various methods for the contact interface exist. These include contact interface by press fit [42], screwing bolts into 3D-printed contact terminals [43], 3D printing over electrical component pads [43], filament deposition and remelting [44], contacting using silver paste [45], using conductive epoxy [46], electroplating 3D-printed conductive paths and soldering components onto them [46], and coating 3D-printed conductive paths with silver paste and depositing copper tape with pre-soldered wires [19,22]. When designing a connection interface between the 3D-printed conductive paths and the measurement cables for 3D-printed PE sensors, EMI shielding must also be considered to improve the signal-to-noise ratio for the charge measurements [19].

In the field of ME, research on EMI shielding has been conducted mostly in the X-band region [47]. In 2021, Schmitz and colleagues [48] reported that SE depends on the printing pattern and the composition of the polymer material, while Lee and colleagues [49] investigated the influence of sample thickness on SE in graphene polyamide 6 (GC). In 2022, Abedi et al. studied the effect of fiber orientation and the number of layers on the SE of low-melt polyaryletherketone (LM PAEK) and continuous-carbon-fiber (CCF) composites fabricated using ME. It was found that SE has a linear relation with the number of layers [50]. In the field of ME and EMI shielding the research on the lower-frequency region, where 3D-printed PE sensors operate, is limited. In order to effectively shield a 3D-printed PE sensor from EMI, it is necessary to shield all further connections to the measurement equipment, including the 3D-printed wires and connection interfaces between the 3D-printed wires and the shielded cables.

Building on the ME and electrode-based poling technique [19], where no EMI-protection was implemented, and the effect of electrode resistance on the response of 3D-printed piezoelectric sensors [41], this manuscript introduces design principles for fabricating EMI-protected, fully 3D-printed piezoelectric sensors in a single process. It addresses the challenges of the fabrication and electrode-based poling processes in adding EMI protection, and presents a connection interface design for integrating the 3D-printed sensor with commercial measurement instruments. In addition, the sensor is presented in a force-measurement application, where EMI noise suppression is shown.

2. Theoretical background

The piezoelectric response for a 3D-printed piezoelectric film is defined by the 3D-print pattern [19], as seen in Fig. 1. The direct piezoelectric effect is sufficient when a piezoelectric material is used as a sensor to measure mechanical stress [41]. If the electrodes are

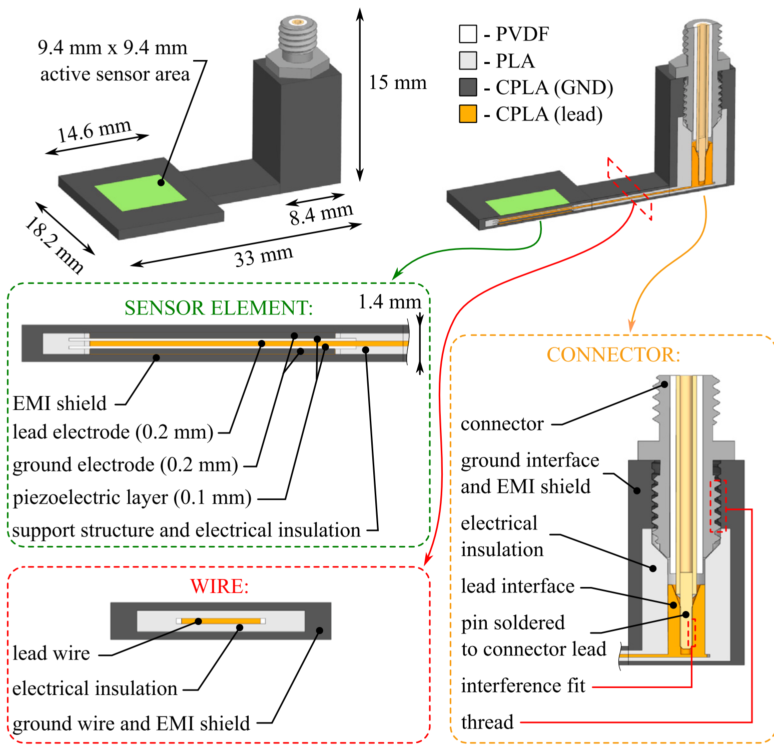

Fig. 2. Single-process 3D-printed piezoelectric sensor design. (For interpretation of the references to color in this figure legend, the reader is referred to the web version of this article.)

arranged on the PE film in the direction of a thickness (axis 3) and by assuming that the in-plane electric fields E_2 and E_3 are negligible, see Fig. 1, the direct piezoelectric effect is:

$$D_3 = d_{31}\,\sigma_1 + d_{32}\,\sigma_2 + d_{33}\,\sigma_3 + \xi^{\sigma}_{33} E_3 \tag{1}$$

where D_3 is the electric displacement in axis 3, σ_1, σ_2 and σ_3 are mechanical stresses in axes 1, 2 and 3, respectively, d_{31}, d_{32}, d_{33} are the piezoelectric strain coefficients, E_3 is the electric field in direction 3 and ξ^{σ}_{33} is permittivity constant at constant mechanical stress. With negligible electrode resistance and charge measurement with a charge amplifier, no electric field is generated in the PE film, hence $E_3 = 0$. The charge collected at the electrodes in the case of a mechanical stress measurement is [51]:

$$q = \int_A D_3 \,\mathrm{d}A \tag{2}$$

where A is the electrode area. For further details on the piezoelectric effect, the interested reader is referred to [19,41].

3. Sensor design

The 3D-printed piezoelectric (3DP PE) sensor is designed to measure electrical charge under time-varying loads, taking into account aspects such as manufacturing technology, EMI shielding, and electric poling. It is fabricated in a material extrusion (ME) process with thermoplastic polymer from three different commercially available materials: PVDF from Nile Polymers, Prusament PLA from Prusa Reserach and CPLA containing carbon black from Protopasta. After the fabrication step, the 3DP PE sensor is poled on the 3D printer build surface by applying a high voltage to the 3D-printed electrodes as described in more detail in Section 4.2. The sensor consists of a 3D-printed piezoelectric sensing element, a 3D-printed wire, and a 3D-printed connector interface.

Fabricating the 3D-printed PE sensor in a single process presents several challenges, including avoiding short circuits between the electrodes during fabrication and preventing arcing during the electric poling [19]. To avoid short circuits, the ME process must ensure that the conductive and non-conductive materials do not mix. Another problem in the fabrication of 3DP PE sensors is arcing during the electrode-based poling [19]. Small imperfections in the PE film decrease the maximum achievable electric poling fields, which reduces the sensor's sensitivity. Electrode-based poling in oil can increase the electric poling fields by filling potential imperfections [25]; however, this is not possible for sensors 3D-printed in a single process, since the poling process takes place immediately after or during the printing and the sensor might be embedded in different structures, e.g., an EMI shield. EMI shielding made of conductive material can effectively reduce the noise; however, constructing EMI shielding around the sensor increases the inactive portion of the sensing element and increases the overall dimensions of the sensor. In addition, suitable electrical insulation must be printed between the cage and the lead electrode and wire to prevent breakdown during the poling process while minimizing the size of the 3DP PE sensor.

The following paragraphs detail how 3D-printed sensing elements (Section 3.1), the 3D-printed wire (Section 3.2) and the 3D-printed connector interface (Section 3.3) address the challenges of: (a) EMI shield placement, (b) preventing electrode short circuits, and (c) eliminating arcing during electrode-based poling, as previously discussed.

3.1. 3D-printed piezoelectric sensing element

As shown in Fig. 2, the 3D-printed piezoelectric sensing element consists of two extruded 3D-printed piezoelectric PVDF films (white color) contacted with a 3D-printed CPLA lead (orange color) and the ground electrodes (dark gray color). The 3D-printed lead electrode is connected to the 3D-printed lead wire and the 3D-printed ground electrodes are connected to the 3D-printed EMI shield, which also serves as the ground contact. By using two 3D-printed piezoelectric PVDF films, the 3D-printed ground electrodes can be placed on the outer surfaces of the two PVDF PE films and easily connected to the EMI shield and ground. When designing the 3D-printed PE sensor element for ME, the extruded PVDF film should be longer in the printing direction compared

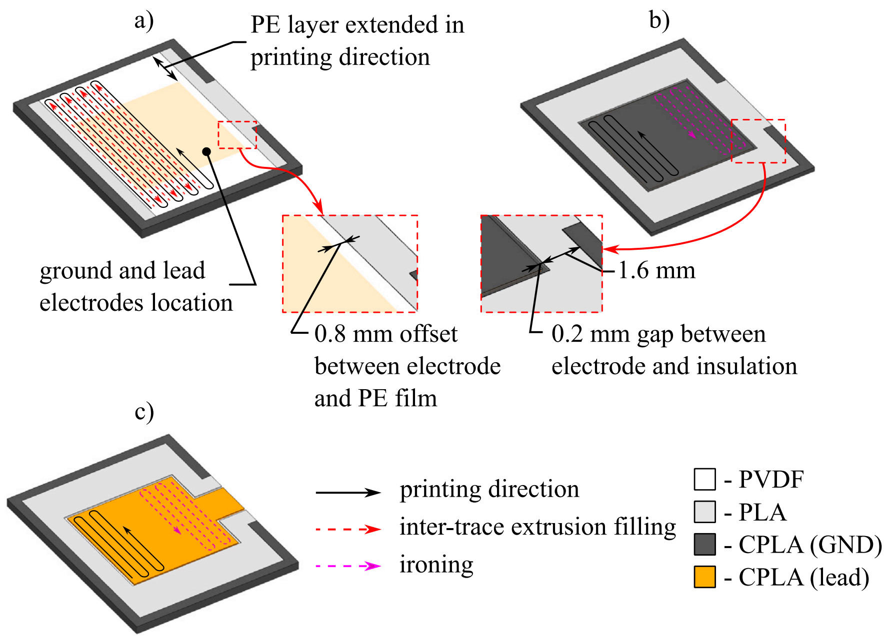

Fig. 3. Details of the functional 3D-printed PE sensor layers: (a) top and bottom piezoelectric film layer, (b) top and bottom ground electrodes, (c) lead electrode layer.

to the active area contacted by the 3D-printed electrodes, see Fig. 3(a); the reason for this is to ensure that the active PE area is free of air gaps and that the PVDF film is firmly bonded to the PLA support structure from all sides [19].

To reduce the risk of air gaps between the extruded PVDF traces in the 3D-printed PE film, a novel inter-trace extrusion-filling process was introduced. Inter-trace extrusion filling is a process that follows the deposition of the PE layer, in which the 3D printer's nozzle is positioned between the deposited PE traces and additional PVDF material is extruded at a reduced extrusion rate, see Fig. 3(a). The purpose of the additional material is to fill possible gaps in the film and ensure a more uniform structure. In addition, the inter-trace extrusion-filling process between the traces helps to smooth the PE layer, resulting in a more uniform and smoother surface. Further details are presented in Section 4.1

To minimize the risk of arcing, the 3D-printed lead and ground CPLA electrodes are offset by approximately 0.8 mm from the edges of the PE film, see the detail of Fig. 3(a). A 1.6-mm-wide PLA insulation (4 perimeters) is printed between the 3D-printed lead electrode and the EMI shield to prevent arcing and to mechanically support the 3D-printed PE layers, see Fig. 3(b). The 3D-printed CPLA electrodes are ironed using the printer nozzle to ensure a smooth deposition surface for the subsequent PE layer. A gap of 0.2 mm is maintained between all the 3D-printed CPLA electrodes and the insulation on all sides (see Fig. 3) to facilitate the filling of excess material from the ironing process and prevent the mixing of materials.

3.2. 3D-printed wire

The 3D-printed conductive wire connecting the 3D-printed sensing element to the 3D-printed connector interface must be of sufficient cross-section to keep its electrical resistance low. Additionally the ground wire should completely enclose the lead wire as an EMI shield. The PLA insulation between the CPLA wires should be at least 1.6 mm (4 perimeters) wide in the layer plane and 0.4 mm (2 layers) thick in the Z direction to prevent arcing. As with 3D-printed electrodes, a gap of 0.4 mm should be maintained between the CPLA wires and the PLA insulation in the printing plane to prevent the mixing of the insulation and conductive materials.

3.3. 3D-printed connector interface

The design of the 3D-printed connector interface facilitates the attachment of a commercial UNF 10–32 connector. This connector, equipped with a soldered copper pin as a lead extension, is screwed into the 3D-printed PE sensor's interface, as shown in Fig. 2. With this the 3D-printed sensor can be connected to commercial cables typically used in PE sensing. The 3D-printed connector interface comprises a conductive lead interface constructed from CPLA, a conductive ground interface made from CPLA that functions as an EMI shield, a 3D-printed ground material connection, and has a 3D-printed thread for screwing and securing the connector. The electrical insulation is thick enough to withstand the poling process. The conductive lead interface is connected to the lead connector extension via an interference fit during the screwing process. To ensure good electrical contact and prevent breakage of the 3D-printed connector interface, the connector is screwed into the 3D-printed interface immediately after the 3D-printing process while the material is still at about 60 °C.

4. Experimental methods

4.1. Sensor fabrication

The PE sensor was fabricated using the E3D Toolchanger with four Matrix extruder tools from Trianglelab, each with a nozzle diameter of 0.4 mm. The PVDF layers were printed with a layer height of 0.1 mm, while the electrodes, wires and other support structures were printed with a layer height of 0.2 mm. The temperature of the print bed was set to 60 °C during the 3D-printing process. The g-code file for the sensor was created using Prusa Slicer 2.5.0, and custom features, including ironing of the electrodes and wires and inter-trace extrusion filling to the PE layers, were added using in-house-developed Python libraries. The electrodes were ironed at a speed of 55 mm/s at a 0% extrusion rate and a spacing of 0.2 mm, while the inter-trace extrusion filling to the PE layers was deposited at a speed of 17 mm/s at 55% of the original extrusion rate to minimize the air gaps in the PE layers. Brims were used to prevent warping due to the high coefficient of thermal expansion of PVDF, as observed in [19]. A draft shield (see Fig. 5) was 3D-printed around the 3DP PE sensor to achieve proper polymer

Fig. 4. 3DP PE sensor after fabrication: (a) 3DP PE sensor with full EMI shield, (b) 3DP PE sensor with partial EMI shield.

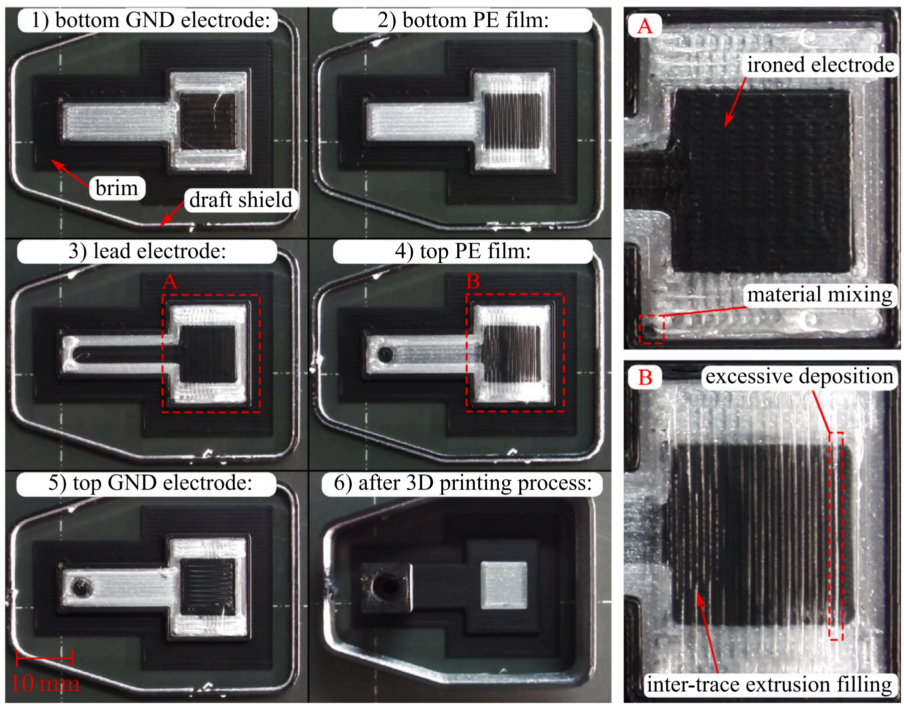

Fig. 5. 3DP PE sensor during fabrication.

flow in the 3D printer's nozzle before printing the sensor to reduce the number of defects on the sensor. The entire 3D-printing process took approximately 40 min. After printing, the UNF 10–32 threaded connector was attached while maintaining the temperature of the print bed at 60 °C. Destructive tests revealed a variation of 130–620 ohms in the resistance between the commercial UNF 10–32 connector and the 3D-printed connection interface for both lead and ground connections. After attaching the connector, the PE sensor was ready for the poling process.

An example of a fabricated 3DP PE sensor is shown in Fig. 4(a), and its internal structure can be seen in Fig. 5, where selected 3D-printed layers during the fabrication process are shown. The two PE layers have a slight excess of material due to the inter-traces extrusion filling. The lead electrode and the two ground electrodes were 3D printed without defects. Only slight material mixing was observed between the EMI shielding made of CPLA and the electrical insulation made of PLA, manifested as black spots on the gray electrical insulation. The same observations were made with other 3D-printed PE sensors. A total of four functional 3DP PE sensors were printed, three with full EMI shielding, see Fig. 4(a), and one with partial EMI shielding, see Fig. 4(b), which was used for the noise comparison described in Section 4.4 (see Table 1).

Table 1
Print parameters for ME of the piezoelectric sensor.

Filament type	Movement speed [mm/s]	Extrusion factor [%]	Cooling setting [%]	Extrusion width [mm]	Nozzle temperature [°C]
PLA	20	99	100	0.4	215
PVDF	17	120	0	0.4	200
CPLA	20	93	100	0.4	215

4.2. Electrode-based poling

During the poling process, high-voltage direct current (HVDC) is applied to the two PE layers of the sensor. To avoid arcing, the positive terminal of the HVDC converter (Ultra 15AV12-P4, Advanced Energy) is connected to the sensor connector lead terminal using a custom adapter, see Fig. 6. The custom adapter, which was 3D-printed with a UNF female thread, included a centrally inserted steel pin connected to the lead terminal of the UNF connector, and air gaps were eliminated by filling them with hot glue to prevent arcing. The negative terminal of the HVDC converter is connected to the EMI shield using copper tape.

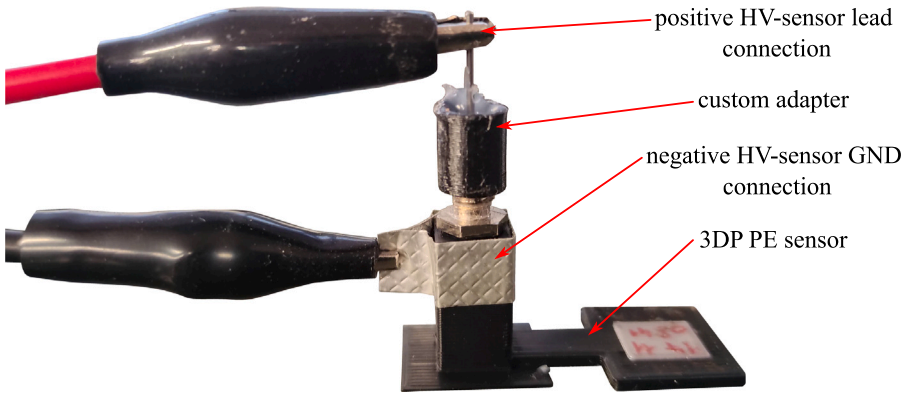

Fig. 6. Poling process of 3DP PE sensor.

The poling process follows the same procedure as described in [19]. The 3DP PE sensors were poled at a temperature of 85 °C, with a maximum voltage of 2.5 kV (electric field of 25 MV/m), as this is the highest value the sensor can reliably withstand without arcing. After the sensor was successfully poled, it was removed from the 3D-printer bed and the 3D-printed brims are removed.

4.3. Usable frequency range

The usable frequency range of a 3DP PE sensor is determined by its electrical and structural properties [41]. From a structural point of view, the usable frequency range is primarily defined by the first natural frequency of the entire sensor assembly, which includes the sensor itself and its mounting components [52]. To ensure a measurement response with excluded sensor's structural dynamics, it is important that the 3DP PE sensor operates well below its first natural frequency. Since the first natural frequency depends on the specific sensor application, the dynamic characteristics of the sensor are not investigated here.

As discussed by Košir and Slavič [41], the usable frequency range of 3DP PE sensors, limited by their electrical characteristics, can be obtained by measuring the transfer function between the collected and generated charge $H(s)$, defined as [41]:

$$H(s) = \frac{Q_{eq}(s)}{Q_{mech}(s)} = \frac{Z_C(s)}{Z_{eq}(s)} \tag{3}$$

where $Q_{eq}(s)$ is the collected charge, $Q_{mech}(s)$ is the total generated charge due to mechanical stresses, Z_{eq} is the electrical impedance of a 3DP PE sensor, Z_C is the impedance of an ideal PE sensor and s is the Laplace complex variable. Based on $H(s)$, the 3 dB low-pass cutoff frequency can be determined. Here, the impedance of the 3DP PE sensor $Z_{eq}(s)$ was measured with Digilent's Analog Discovery 2 using the impedance analyzer module. The impedance $Z_C(s)$ of an ideal PE sensor with equal capacitance to the 3DP PE sensor and negligible resistance was calculated based on the measured 3DP PE sensor capacitance C_{tot}:

$$Z_C(s) = \frac{1}{s\,C_{tot}} \tag{4}$$

The total 3DP PE sensor capacitance C_{tot} was estimated based on the sensor impedance Z_{eq} up to 6 kHz, where the 3DP PE sensor acts as an ideal capacitor (constant phase angle of 90°). Based on $Z_{eq}(s)$ and $Z_C(s)$, $H(s)$ can be estimated using Eq. (3). The Z_{eq} measurement used an open-loop impedance measurement to compensate for the cable capacitance used to connect the 3DP PE sensor to the impedance module.

4.4. Showcase: Force sensor

To demonstrate the ability of the 3DP sensor PE to measure force, it was showcased as a force sensor. The 3DP sensor was attached to the mounting plate of an electromagnetic shaker (LDS V555) using superglue. An inertial mass with an attached accelerometer (Dytran 3225F7, type ICP) was added to the sensor as shown in Fig. 7. The total mass of the inertial mass and the accelerometer was 25.45 g. In addition, a reference accelerometer (PCB T333B30, type ICP) was attached to the mounting plate of the shaker, as a reference and feedback control. The shaker was excited with a sinusoidal sweep with a constant amplitude of 2 g and a frequency range of 250–1000 Hz. During the excitation, the charge of the 3DP sensor, the acceleration of the mounting plate, and the acceleration of the inertial mass were measured. Knowing the total inertial mass m and the acceleration $a_{\mathrm{mass}}(t)$ of the inertial mass, the force $F(t)$ applied to the 3DP sensor can be calculated as follows:

$$F(t) = m\, a_{\mathrm{mass}}(t) \tag{5}$$

The 3DP PE sensor was therefore loaded with a force amplitude of about 0.5 N (the equivalent pressure applied to the active surface of the sensor is therefore about 5660 Pa). The sensitivity of the 3DP PE force sensor can be identified in the frequency domain as [19]:

$$K(f) = \frac{S_{qF}(f)}{S_{FF}(f)}, \tag{6}$$

where $S_{qF}(f)$ is the cross-spectral density of the charge $q(t)$ and the force $F(t)$, $S_{FF}(f)$ is the power spectral density of the force $F(t)$, and $K(f)$ is the 3DP PE sensor's sensitivity. The response of the 3DP PE sensor with negligible structural dynamic effects is expected significantly below the first natural frequency. The first natural frequency is identified from the transmissibility $T(f)$:

$$T(f) = \frac{S_{a_1 a_2}(f)}{S_{a_2 a_2}(f)}, \tag{7}$$

where $S_{a_1 a_2}(f)$ is the cross spectral density of the mounting plate's acceleration a_{base} and the inertial mass' acceleration a_{mass}, $S_{a_2 a_2}(f)$ is the power spectral density of the inertial mass acceleration a_{mass}.

The charge generated on the 3DP PE sensor was measured using Brüel & Kjær's Nexus 2692 charge amplifier connected to the DAQ input card NI 9234. Accelerations on the shaker mounting plate and the inertial mass were measured using accelerometers connected directly to the DAQ input board NI 9234 at a sampling rate of 25.6 kHz. The charge amplifier was used with a high-pass filter at 0.1 Hz. Four 3DP PE sensors were tested using the proposed method, three with a full EMI shield and one with a partial EMI shield.

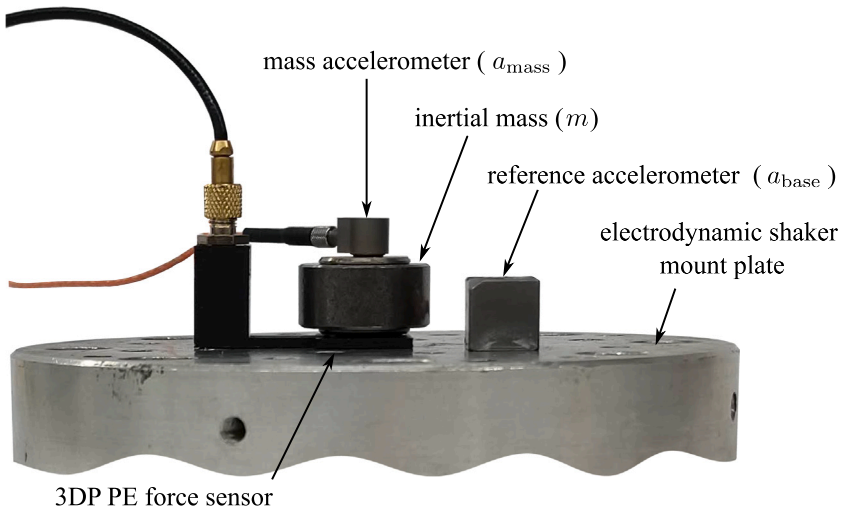

Fig. 7. Sensitivity measurement of 3DP PE sensor, showcased as a force sensor.

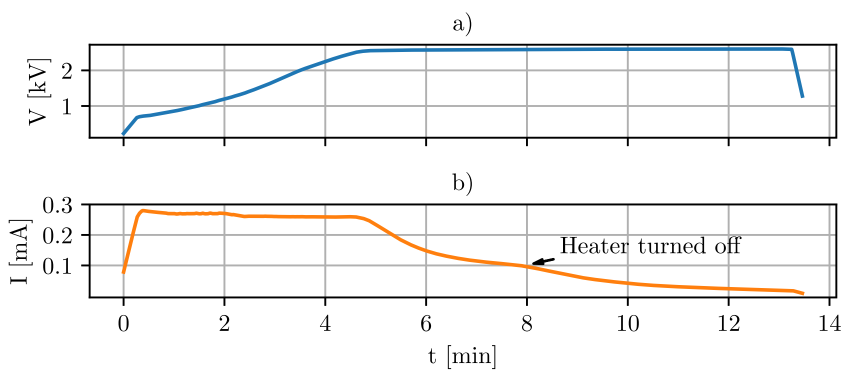

Fig. 8. Example of electric poling profile used on 3DP PE sensor.

5. Results

5.1. Electric poling

Fig. 8 shows an example of a successful poling process. After reaching a steady-state temperature field, the process is current-controlled and, after reaching the final poling voltage of 2.5 kV, voltage-controlled. The point at which the bed heater was turned off (after about 8 min of poling) can be observed as the poling current decreases even more steeply. The electric poling field was 25 MV/m and is lower than the PVDF coercive electric field of about 43 MV/m as reported in [53] for a temperature of 85°C. Increasing the electric field caused arcing and made the fabrication of the sensor unreliable.

5.2. Usable frequency range

Fig. 9(a) and (c) show the measured electrical impedances of the four 3DP PE sensors. Based on the measured electrical impedances, the transfer function between the collected and generated charge, $H(s)$ (see Eq. (3)), is calculated as shown in Fig. 9(b) and (d). The measured 3 dB low-pass cutoff frequencies are 237 kHz, 243 kHz, 223 kHz and 199 kHz for samples 1, 2, 3, and 4 (partial EMI shielding), respectively. Therefore, the electrical characteristics will not significantly affect the sensory function up to 20 kHz. The average capacitance of the 3DP PE sensor assembly, averaged over the frequency range up to 6 kHz, is 138 pF with full EMI shielding. For the 3DP PE sensor with partial EMI shielding, a capacitance of 119 pF was measured.

5.3. Showcase: Force sensor

Fig. 10 presents the time- and frequency-domain representations of the excitation force F, as measured by the inertial mass using a commercial accelerometer (Dytran 3225F7). In Fig. 10(a), the time-domain measurements at a frequency of 300 Hz are depicted, while Fig. 10(b) illustrates the excitation force's frequency content. Fig. 11 shows time- and frequency-domain representations of the charge q, as detected by two 3DP PE sensors with comparable sensitivity (with full and partial EMI shielding). Observations reveal a substantial reduction in the electromagnetic interference with the implementation of full EMI shielding. The charge captured by the 3DP PE sensor with partial EMI shielding contains noise with a base harmonic of 50 Hz, whereas the charge measured by the 3DP PE sensor with full EMI shielding exhibits considerably less noise. To quantify the noise reduction, the signal-to-noise ratio SNR for the measurements shown in Fig. 11 was calculated as follows:

$$SNR = 10 \log \frac{P_{signal}}{P_{noise}} \tag{8}$$

where P_{signal} is the signal power at 300 Hz and P_{noise} is the signal power at all other frequencies. For the 3DP PE sensor with partial EMI shielding, SNR was found to be 3.5 dB and for the 3DP PE sensor with full EMI shielding, SNR was found to be 27.2 dB. The noise was thus reduced by a factor of 234.

From the measured transmissibility $T(f)$ (see Eq. (7)), the natural frequencies identified for all the 3DP PE sensors, when attached to

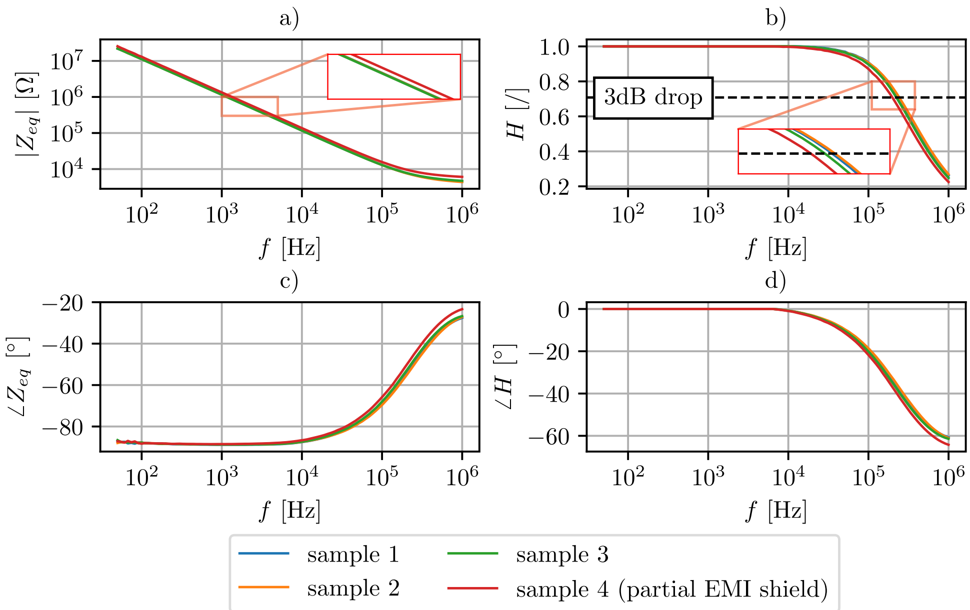

Fig. 9. Measured impedance Z_{eq} and transfer function H: (a) Z_{eq} amplitude spectrum, (b) H amplitude spectrum, (c) Z_{eq} phase spectrum, (d) H phase spectrum.

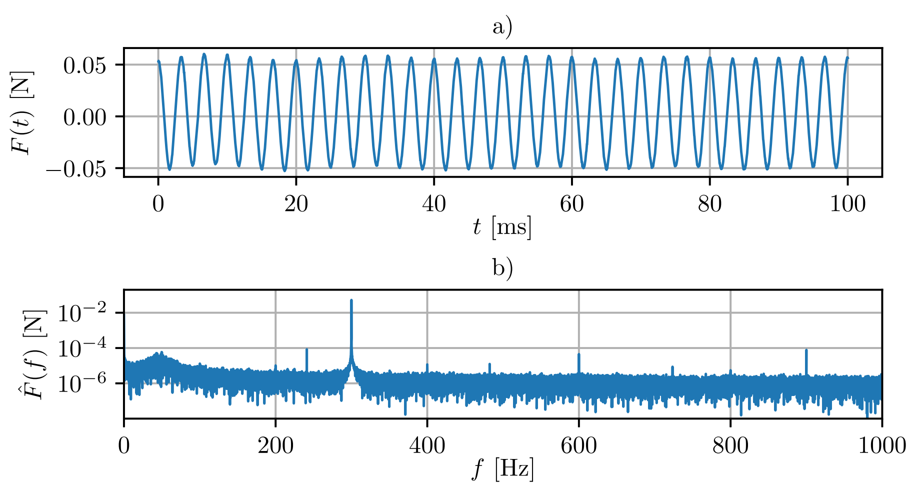

Fig. 10. Measured excitation force $F(t)$ at 300 Hz: (a) $F(t)$ time signal, (b) force amplitude spectrum $\hat{F}(f)$.

an inertial mass, surpassed 3000 Hz. Referring to the one-dimensional spring-mass model theory [52], the system's response should not notably impact on the measured sensor sensitivities $K(f)$ for up to one-third of the natural frequency. As a result, the sensitivity $K(f)$ was measured up to 1000 Hz, where the effects of the dynamics of the test setup can be deemed negligible.

Fig. 12 displays the sensitivities $K(f)$ for 3DP PE sensors with full EMI shielding. The amplitude spectrum of the 3DP PE sensor's sensitivity $K(f)$, seen in Fig. 12(a), indicates a consistent sensitivity throughout the evaluated frequency range. As expected, the phase spectrum of the sensitivity $K(f)$ in Fig. 12(b) demonstrates no significant phase delay between the excitation force and the generated charge for all samples. Fig. 12 also highlights that, due to fabrication repeatability, the sensitivity of the 3DP PE sensors, poled at the same conditions, varies between 0.71 pC/N and 0.89 pC/N, when employed as force sensors. If normed to charge per unit area, the sensitivity of the 3DP force sensor varies between approximately $6.3 \cdot 10^{-5}$ pC/Pa and $7.9 \cdot 10^{-5}$ pC/Pa.

6. Discussion

While the adhesion between PLA and PVDF showed good integrity, as indirectly confirmed in [19], weaker bonding between PVDF and CPLA was also observed in the study, making the CPLA layer susceptible to detachment from the PVDF layer. Nevertheless, the structural robustness of the 3DP PE sensor was maintained for all samples during the presented measurements, likely due to the complete encapsulation of the PVDF layers, which was further supported by PLA structures and insulation (see Fig. 2). The risk of delamination could occur at higher tensile loads in the direction of the PVDF film thickness, but this is beyond the scope of this study.

The duration of the electrode-based poling process was mostly limited by the maximum electric current that could be supplied by the HVDC converter. A higher electric current supplied by the high-voltage DC/DC converter can accelerate the electrode-based poling process. However, this would result in an increase in the temperature and the likelihood of arcing between the lead and ground electrodes [19]. The

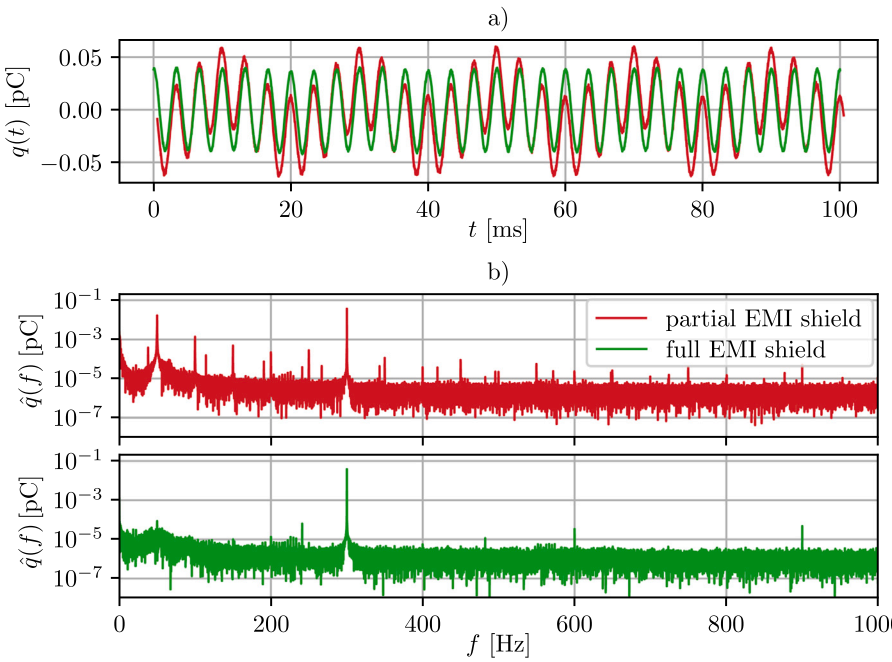

Fig. 11. Measured charge by two 3DP PE sensors with full and partial EMI shielding at 300 Hz: (a) time signal $q(t)$, (b) charge amplitude spectrum $\hat{q}(f)$.

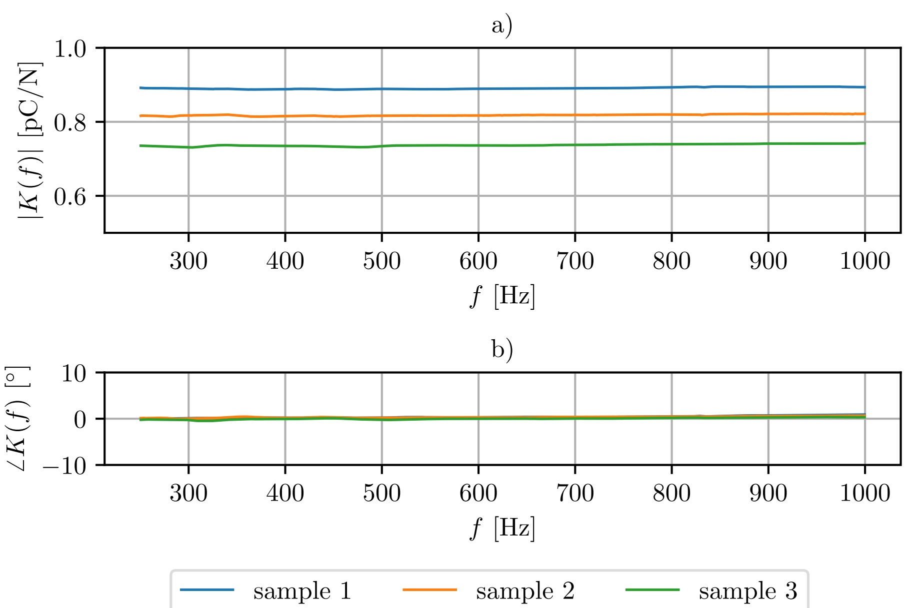

Fig. 12. Measured sensitivity $K(f)$ of 3DP PE sensors with full EMI shield: (a) $K(f)$ amplitude spectrum, (b) $K(f)$ phase spectrum.

3D-printed piezoelectric sensors that underwent a successful poling process exhibited an electrical resistance between electrodes exceeding 50 MΩ, which was the limit of our measurement equipment. Electric poling with electric fields higher than the coercive field of PVDF is currently not possible, as arcing occurs between the lead and ground electrodes. Arcing can occur through the PE layer or 3D-printed electrical insulation. The location of the arcing is difficult to determine, as it occurs inside the sensor assembly. In most cases, arcing results in a short circuit of the electrodes, with electrical resistance between the lead and ground electrodes ranging from a few kilo-ohms to mega-ohms at room temperature. Increasing the electric field above 3 kV tends to result in arcing at the connector interface and the 3D-printed wires.

Adding EMI shielding to all 3DP PE sensor components increases the sensor's capacitance, effectively resulting in a lower 3 dB low-pass cutoff frequency and thus a lower usable frequency range. It should be noted that other measurement components, such as cables and charge amplifiers, further increase the capacitance of the measurement system and reduce the usable frequency range. The 3 dB low-pass cutoff frequency of the 3DP PE sensor, due to its electrical properties, was found to range from 199 kHz to 243 kHz. Below the cutoff frequency, the effect of electrode resistance on collected charge can be neglected [41]. Therefore, the usable frequency range of the 3DP PE sensor is most likely to be determined by its structural characteristics and the manner in which it is embedded into the smart structure. Measurements in mechanical engineering are usually below 20 kHz; however, the usable frequency range depends on the application and was therefore not investigated in detail here.

The level of noise measured by the 3DP PE sensor with partial EMI shielding depends on the measurement setup, such as the grounding of the measurement chain, the use of a PC with a battery or connected to a power supply, and the physical contact with the measurement unit. However, regardless of the measurement setup, noise was always significantly reduced in the 3DP PE sensor with full EMI shielding compared to the sensor with partial EMI shielding.

During the sensitivity measurements, the connection between the 3DP PE force sensor and the measurement equipment proved to be stable, with no signal spikes or interruptions observed in the acquired time signals of the charge measurements that could indicate a poor connection. Manual loading of the connection interface did result in measured charge signals, which is to be expected since mechanical stresses are also induced in the piezoelectric layers when the connection interface is loaded; however, the charge readings were at least an order of magnitude lower than those measured when the same force was applied to the actual measurement area. The sensitivity of the force sensor with EMI protection was slightly lower than that of the single-process 3D-printed piezoelectric sensor (without EMI protection) reported in [19], although here a configuration with two PE layers was used, which should theoretically double the sensor's sensitivity in the PE layer's thickness direction compared to a sensor with a single PE layer. The lower sensitivity can be partially addressed to the fact that a significant portion of the force is transmitted through the EMI shielding and electrical insulation rather than through the active PE sensing element. Nevertheless, the signal-to-noise ratio of the sensor is much higher than the 3D-printed PE sensor presented in [19].

The sensor also responded well to load directions other than those presented in this manuscript. If force or strain measurements are desired in only one direction, an additional structure should be designed around the presented 3DP PE sensor to ensure measurement in the desired direction.

The 3D-printed PE sensor, with a sensitivity of $0.71-0.89\,\mathrm{pC/N}$, is 30–40 times less sensitive than commercial PVDF sensors ($23-33\,\mathrm{pC/N}$) [54]; however, its integrated EMI shielding, uncommon in conventional sensors, significantly reduces noise and enables accurate measurements in high-noise environments, such as electromagnetic actuators [17]. In addition, 3DP PE sensors have several unique advantages over their conventional counterparts. First, their fabrication can be done in a single process using a 3D printing machine, which is a significant difference from the multi-step processes required to fabricate conventional PE sensors. 3DP PE sensors can be embedded directly into a variety of structures in a single process, creating opportunities for fabricating "smart" structures with sensory feedback that are useful for a range of applications, from vibration control [55], health monitoring of structures [4], human health monitoring [56] and metamaterials [57, 58].

7. Conclusions

This manuscript introduces the design principles for the fabrication of a single-process 3D-printed and EMI-protected piezoelectric (PE) sensor using the material extrusion (ME) approach with thermoplastic polymer. The design principles describe how to design a 3D-printed piezoelectric sensing element, 3D-printed wires, and a 3D-printed connector interface, all designed to provide effective EMI shielding, prevent electrode short-circuiting, and eliminate arcing during the electrode-based poling.

To prevent electrode short-circuiting and arcing an inter-trace extrusion-filling process should be utilized. Material mixing can be prevented by maintaining a small air gap between the electrode and the insulation, and smoothing out the electrodes using the ironing process. The 3D-printed connector interface makes it possible to attach a commercial UNF 10–32 connector to the 3D-printed PE sensor.

The usable frequency range of the sensor, due to its electrical properties and low-pass filtering characteristics, was measured, and 3 dB low-pass cut-off frequencies between $199\,\mathrm{kHz}$ and $243\,\mathrm{kHz}$ were obtained for different samples.

Electromagnetic interference suppression was compared for the 3D-printed PE sensor with partial and full EMI shielding, and the noise was reduced by a factor of 234.

The performance of a 3DP PE sensor was evaluated as a force sensor. The measured sensitivity of the 3D-printed PE sensor was between $0.71\,\mathrm{pC/N}$ and $0.89\,\mathrm{pC/N}$ and a signal-to-noise ratio was found to be $27.2\,\mathrm{dB}$.

CRediT authorship contribution statement

Tilen Košir: Writing – review & editing, Writing – original draft, Visualization, Validation, Software, Methodology, Formal analysis, Data curation, Conceptualization. **Janko Slavič:** Writing – review & editing, Writing – original draft, Validation, Supervision, Resources, Project administration, Methodology, Investigation, Funding acquisition, Formal analysis, Conceptualization.

Declaration of competing interest

The authors declare that they have no known competing financial interests or personal relationships that could have appeared to influence the work reported in this paper.

Data availability

Data will be made available on request.

Acknowledgments

The authors gratefully acknowledge partial financial support from the Slovenian Research Agency (core funding of research No. P2-0263 and research project J2-3045).

References

[1] E. MacDonald, R. Wicker, Multiprocess 3D printing for increasing component functionality, Science 353 (6307) (2016) aaf2093, http://dx.doi.org/10.1126/science.aaf2093, arXiv:https://www.science.org/doi/pdf/10.1126/science.aaf2093. URL https://www.science.org/doi/abs/10.1126/science.aaf2093.

[2] E. MacDonald, D. Espalin, D. Doyle, J. Muñoz, S. Ambriz, J. Coronel, A. Williams, R. Wicker, Fabricating patch antennas within complex dielectric structures through multi-process 3D printing, J. Manuf. Process. 34 (2018) 197–203, http://dx.doi.org/10.1016/j.jmapro.2018.05.013, URL https://www.sciencedirect.com/science/article/pii/S152661251830505X.

[3] M.A. Ali, C. Hu, E.A. Yttri, R. Panat, Recent advances in 3D printing of biomedical sensing devices, Adv. Funct. Mater. 32 (2022) http://dx.doi.org/10.1002/adfm.202107671.

[4] A.V. Gaumet, R.J. Ball, A. Nogaret, Graphite-polydimethylsiloxane composite strain sensors for in-situ structural health monitoring, Sensors Actuators A 332 (2021) 113139, http://dx.doi.org/10.1016/j.sna.2021.113139, URL https://www.sciencedirect.com/science/article/pii/S092442472100604X.

[5] A. Kalkal, S. Kumar, P. Kumar, R. Pradhan, M. Willander, G. Packirisamy, S. Kumar, B.D. Malhotra, Recent advances in 3D printing technologies for wearable (bio)sensors, Addit. Manuf. (2021) 102088, http://dx.doi.org/10.1016/j.addma.2021.102088, URL https://www.sciencedirect.com/science/article/pii/S2214860421002530.

[6] F. Mashayekhi, J. Bardon, S. Westermann, F. Addiego, Adhesion optimization between incompatible polymers through interfacial engineering, Polymers 13 (24) (2021) http://dx.doi.org/10.3390/polym13244273, URL https://www.mdpi.com/2073-4360/13/24/4273.

[7] M.R. Khosravani, T. Reinicke, 3D-printed sensors: Current progress and future challenges, Sensors Actuators A 305 (2020) 111916, http://dx.doi.org/10.1016/j.sna.2020.111916, URL https://www.sciencedirect.com/science/article/pii/S0924424720300868.

[8] V. Zega, M. Invernizzi, R. Bernasconi, F. Cuneo, G. Langfelder, L. Magagnin, M. Levi, A. Corigliano, The first 3D-printed and wet-metallized three-axis accelerometer with differential capacitive sensing, IEEE Sens. J. 19 (20) (2019) 9131–9138, http://dx.doi.org/10.1109/JSEN.2019.2924473.

[9] G.L. Goh, H. Zhang, T.H. Chong, W.Y. Yeong, 3D printing of multilayered and multimaterial electronics: A review, Adv. Electron. Mater. (2021) 2100445, http://dx.doi.org/10.1002/aelm.202100445.

[10] R. Bernasconi, D. Hatami, H.N. Hosseinabadi, V. Zega, A. Corigliano, R. Suriano, M. Levi, G. Langfelder, L. Magagnin, Hybrid additive manufacturing of a piezopolymer-based inertial sensor, Addit. Manuf. 59 (2022) http://dx.doi.org/10.1016/j.addma.2022.103091.

[11] S.-M. Chang, S. Hur, J. Park, D.-G. Lee, J. Shin, H.S. Kim, S.E. Song, J.M. Baik, M. Kim, H.-C. Song, C.-Y. Kang, Optimization of piezoelectric polymer composites and 3D printing parameters for flexible tactile sensors, Addit. Manuf. (2023) http://dx.doi.org/10.1016/j.addma.2023.103470, URL https://linkinghub.elsevier.com/retrieve/pii/S2214860423000830.

[12] S. Bodkhe, C. Noonan, F.P. Gosselin, D. Therriault, Coextrusion of multifunctional smart sensors, Adv. Eng. Mater. 20 (2018) http://dx.doi.org/10.1002/adem.201800206.

[13] H. Li, S.-W. Jin, J.H. Lim, S. Lim, Solvent-assisted precipitation direct-write printing toward in-suit oriented beta-phase polyvinylidene fluoride with tunable microarchitectures for energy harvesting and self-powered sensing, Appl. Mater. Today 29 (2022) 101633, http://dx.doi.org/10.1016/j.apmt.2022.101633, URL https://www.sciencedirect.com/science/article/pii/S2352940722002670.

[14] Z. Wang, Y. Wu, B. Zhu, Q. Chen, L. Wang, Y. Zhao, D. Sun, J. Zheng, D. Wu, A magnetic soft robot with multimodal sensing capability by multimaterial direct ink writing, Addit. Manuf. 61 (2023) http://dx.doi.org/10.1016/j.addma.2022.103320.

[15] P. Laszczak, L. Jiang, D. Bader, D. Moser, S. Zahedi, Development and validation of a 3D-printed interfacial stress sensor for prosthetic applications, Med. Eng. Phys. 37 (1) (2015) 132–137, http://dx.doi.org/10.1016/j.medengphy.2014.10.002, URL https://www.sciencedirect.com/science/article/pii/S1350453314002537.

[16] D. Thi Ngoc Nga, G. Mattana, V.T. Thu, R. Roussel, B. Piro, A simple flexible printed capacitive pressure sensor for chronic wound monitoring, Sensors Actuators A 338 (2022) 113490, http://dx.doi.org/10.1016/j.sna.2022.113490, URL https://www.sciencedirect.com/science/article/pii/S0924424722001285.

[17] A. Pavone, G. Stano, G. Percoco, One-shot 3D printed soft device actuated using metal-filled channels and sensed with embedded strain gauge, 3D Print. Addit. Manuf. (2023) http://dx.doi.org/10.1089/3dp.2022.0263.

[18] M. Arh, J. Slavič, M. Boltežar, Experimental identification of the dynamic piezoresistivity of fused-filament-fabricated structures, Addit. Manuf. 36 (2020) 101493, http://dx.doi.org/10.1016/j.addma.2020.101493, URL https://www.sciencedirect.com/science/article/pii/S2214860420308654.

[19] T. Košir, J. Slavič, Single-process fused filament fabrication 3D-printed high-sensitivity dynamic piezoelectric sensor, Addit. Manuf. 49 (2022) 102482, http://dx.doi.org/10.1016/j.addma.2021.102482, URL https://www.sciencedirect.com/science/article/pii/S2214860421006291.

[20] C. Lee, J.A. Tarbutton, Electric poling-assisted additive manufacturing process for PVDF polymer-based piezoelectric device applications, Smart Mater. Struct. 23 (9) (2014) 095044, http://dx.doi.org/10.1088/0964-1726/23/9/095044.

[21] C.J. Hohimer, G. Petrossian, A. Ameli, C. Mo, P. Pötschke, 3D printed conductive thermoplastic polyurethane/carbon nanotube composites for capacitive and piezoresistive sensing in soft pneumatic actuators, Addit. Manuf. 34 (2020) 101281, http://dx.doi.org/10.1016/j.addma.2020.101281, URL https://www.sciencedirect.com/science/article/pii/S2214860420306539.

[22] M. Arh, J. Slavič, M. Boltežar, Design principles for a single-process 3d-printed accelerometer – theory and experiment, Mech. Syst. Signal Process. 152 (2021) 107475, http://dx.doi.org/10.1016/j.ymssp.2020.107475, URL https://www.sciencedirect.com/science/article/pii/S088832702030861X.

[23] M. Palmieri, J. Slavič, F. Cianetti, Single-process 3D-printed structures with vibration durability self-awareness, Addit. Manuf. 47 (2021) 102303, http://dx.doi.org/10.1016/j.addma.2021.102303, URL https://www.sciencedirect.com/science/article/pii/S2214860421004619.

[24] G. Stano, S.M.A.I. Ovy, J.R. Edwards, M. Cianchetti, G. Percoco, Y. Tadesse, One-shot additive manufacturing of robotic finger with embedded sensing and actuation, Int. J. Adv. Manuf. Technol. 124 (1) (2023) 467–485, http://dx.doi.org/10.1007/s00170-022-10556-x.

[25] D.A. Porter, T.V. Hoang, T.A. Berfield, Effects of in-situ poling and process parameters on fused filament fabrication printed PVDF sheet mechanical and electrical properties, Addit. Manuf. 13 (2017) 81–92, http://dx.doi.org/10.1016/j.addma.2016.11.005, URL https://www.sciencedirect.com/science/article/pii/S2214860416303281.

[26] H. Li, S. Lim, High-performance piezoelectric nanogenerators featuring embedded organic nanodroplets for self-powered sensors, J. Mater. Chem. A 10 (2022) 14894–14905, http://dx.doi.org/10.1039/D2TA02276A.

[27] A. Jain, K.J. Prashanth, A.K. Sharma, A. Jain, P.N. Rashmi, Dielectric and piezoelectric properties of PVDF/PZT composites: A review, Polym. Eng. Sci. 55 (7) (2015) 1589–1616, http://dx.doi.org/10.1002/pen.24088, arXiv:https://onlinelibrary.wiley.com/doi/pdf/10.1002/pen.24088. URL https://onlinelibrary.wiley.com/doi/abs/10.1002/pen.24088.

[28] J. Fan, D. Gonzalez, J. Garcia, B. Newell, R.A. Nawrocki, The effects of additive manufacturing and electric poling techniques on PVdF thin films: Towards 3D printed functional materials, in: ASME 2020 Conference on Smart Materials, Adaptive Structures and Intelligent Systems, in: Smart Materials, Adaptive Structures and Intelligent Systems, 2020, http://dx.doi.org/10.1115/SMASIS2020-2245.

[29] S.K. Mahadeva, J. Berring, K. Walus, B. Stoeber, Effect of poling time and grid voltage on phase transition and piezoelectricity of poly(vinyledene fluoride) thin films using corona poling, J. Phys. D: Appl. Phys. 46 (28) (2013) 285305, http://dx.doi.org/10.1088/0022-3727/46/28/285305.

[30] N. Momenzadeh, Influences of Material Extrusion Additive Manufacturing (MEAM) Parameters and Additives on Polyvinylidene Fluoride (PVDF) Properties (Ph.D. thesis), University of Louisville, 2020.

[31] H. Kim, F. Torres, Y. Wu, D. Villagran, Y. Lin, T.-L. Tseng, Integrated 3D printing and corona poling process of PVDF piezoelectric films for pressure sensor application, Smart Mater. Struct. 26 (8) (2017) 085027, http://dx.doi.org/10.1088/1361-665x/aa738e.

[32] C. Lee, J. Tarbutton, Polyvinylidene fluoride (PVDF) direct printing for sensors and actuators, Int. J. Adv. Manuf. Technol. 104 (2019) http://dx.doi.org/10.1007/s00170-019-04275-z.

[33] J. Fan, N. Deneke, S. Xu, B. Newell, J. Garcia, C. Davis, W. Wu, R.M. Voyles, R.A. Nawrocki, Electric poling-assisted additive manufacturing technique for piezoelectric active poly(vinylidene fluoride) films: Towards fully three-dimensional printed functional materials, Addit. Manuf. 60 (2022) http://dx.doi.org/10.1016/j.addma.2022.103248.

[34] X. Ye, Z. Hu, X. Li, S. Wang, B. Wang, Y. Zhao, J. He, J. Liu, J. Zhang, Effect of annealing and carbon nanotube infill on the mechanical and electrical properties of additively manufactured polyether-ether-ketone nanocomposites via fused filament fabrication, Addit. Manuf. 59 (2022) 103188, http://dx.doi.org/10.1016/j.addma.2022.103188.

[35] B. Li, S. Zhang, L. Zhang, Y. Gao, F. Xuan, Strain sensing behavior of FDM 3D printed carbon black filled TPU with periodic configurations and flexible substrates, J. Manuf. Process. 74 (2022) 283–295, http://dx.doi.org/10.1016/j.jmapro.2021.12.020.

[36] K. Seetala, W. Clower, C.G. Wilson, Electrochemical enhancement of carbon black-infused poly(lactic acid) filament for additive manufactured electronic applications, Addit. Manuf. 61 (2023) 103283, http://dx.doi.org/10.1016/j.addma.2022.103283.

[37] M. Karimi, A. Asefnejad, D. Aflaki, A. Surendar, H. Baharifar, S. Saber-Samandari, A. Khandan, A. Khan, D. Toghraie, Fabrication of shapeless scaffolds reinforced with baghdadite-magnetite nanoparticles using a 3D printer and freeze-drying technique, J. Mater. Res. Technol. 14 (2021) 3070–3079, http://dx.doi.org/10.1016/j.jmrt.2021.08.084, URL https://www.sciencedirect.com/science/article/pii/S2238785421009121.

[38] T.B. Palmić, J. Slavič, Single-process 3D-printed stacked dielectric actuator, Int. J. Mech. Sci. 230 (2022) 107555, http://dx.doi.org/10.1016/j.ijmecsci.2022.107555, URL https://www.sciencedirect.com/science/article/pii/S0020740322004489.

[39] T.B. Palmić, J. Slavič, Design principles for a single-process 3D-printed stacked dielectric actuators — Theory and experiment, Int. J. Mech. Sci. 246 (2023) 108128, http://dx.doi.org/10.1016/j.ijmecsci.2023.108128, URL https://www.sciencedirect.com/science/article/pii/S0020740323000309.

[40] T. Barši Palmić, J. Slavič, M. Boltežar, Process parameters for FFF 3D-printed conductors for applications in sensors, Sensors 20 (16) (2020) http://dx.doi.org/10.3390/s20164542, URL https://www.mdpi.com/1424-8220/20/16/4542.

[41] T. Košir, J. Slavič, Modeling of single-process 3D-printed piezoelectric sensors with resistive electrodes: The low-pass filtering effect, Polymers 15 (1) (2023) http://dx.doi.org/10.3390/polym15010158, URL https://www.mdpi.com/2073-4360/15/1/158.

[42] S.J. Leigh, R.J. Bradley, C.P. Purssell, D.R. Billson, D.A. Hutchins, A simple, low-cost conductive composite material for 3D printing of electronic sensors, PLoS ONE 7 (2012) e49365, http://dx.doi.org/10.1371/journal.pone.0049365.

[43] N. Lazarus, H.H. Tsang, 3-D printing structural electronics with conductive filaments, IEEE Trans. Compon. Packag. Manuf. Technol. 10 (2020) 1965–1972, http://dx.doi.org/10.1109/TCPMT.2020.3038563.

[44] S.W. Kwok, K.H.H. Goh, Z.D. Tan, S.T.M. Tan, W.W. Tjiu, J.Y. Soh, Z.J.G. Ng, Y.Z. Chan, H.K. Hui, K.E.J. Goh, Electrically conductive filament for 3D-printed circuits and sensors, Appl. Mater. Today 9 (2017) 167–175, http://dx.doi.org/10.1016/j.apmt.2017.07.001.

[45] J. Li, Y. Wang, G. Xiang, H. Liu, J. He, Hybrid additive manufacturing method for selective plating of freeform circuitry on 3D printed plastic structure, Adv. Mater. Technol. 4 (2019) http://dx.doi.org/10.1002/admt.201800529.

[46] N. Lazarus, S.S. Bedair, S.H. Hawasli, M.J. Kim, B.J. Wiley, G.L. Smith, Selective electroplating for 3D-printed electronics, Adv. Mater. Technol. 4 (2019) http://dx.doi.org/10.1002/admt.201900126.

[47] Z. Viskadourakis, K.C. Vasilopoulos, E.N. Economou, C.M. Soukoulis, G. Kenanakis, Electromagnetic shielding effectiveness of 3D printed polymer composites, Appl. Phys. A 123 (12) (2017) 736, http://dx.doi.org/10.1007/s00339-017-1353-z.

[48] D. Schmitz, S. Dul, S. Ramoa, B. Soares, G. Barra, A. Pegoretti, Effect of printing parameters on the electromagnetic shielding efficiency of ABS/carbonaceous-filler composites manufactured via filament fused fabrication, J. Manuf. Process. 65 (2021) 12–19, http://dx.doi.org/10.1016/j.jmapro.2021.02.051, URL https://www.sciencedirect.com/science/article/pii/S1526612521001535.

[49] K.P.M. Lee, T. Baum, R. Shanks, F. Daver, Electromagnetic interference shielding of 3D-printed graphene–polyamide-6 composites with 3D-printed morphology, Addit. Manuf. 43 (2021) 102020, http://dx.doi.org/10.1016/j.addma.2021.102020, URL https://www.sciencedirect.com/science/article/pii/S2214860421001858.

[50] K. Abedi, S. Miri, L. Gregorash, K. Fayazbakhsh, Evaluation of electromagnetic shielding properties of high-performance continuous carbon fiber composites fabricated by robotic 3D printing, Addit. Manuf. 54 (2022) 102733, http://dx.doi.org/10.1016/j.addma.2022.102733.

[51] S.O.R. Moheimani, A.J. Fleming, Piezoelectric Transducers for Vibration Control and Damping, Springer, London, 2006, pp. 1–33.

[52] K.G. McConnell, P.S. Varoto, Vibration Testing: Theory and Practice, John Wiley & Sons, 1995, pp. 169–181.

[53] R. Olsen, J. Hicks, M. Broadhurst, G. Davis, Temperature-dependent ferroelectric hysteresis study in polyvinylidene fluoride, Appl. Phys. Lett. 43 (1) (1983) 127–129, http://dx.doi.org/10.1063/1.94142.

[54] DT Series Elements with Lead Attachments, Tech. rep., TE connectivity, 2017, URL https://www.te.com/commerce/DocumentDelivery/DDEController?Action=showdoc&DocId=Data+Sheet%7FDT_Series_with_Riveted_Leads%7FA1%7Fpdf%7FEnglish%7FENG_DS_DT_Series_with_Riveted_Leads_A1.pdf%7FCAT-PFS0005.

[55] G.M. Chatziathanasiou, N.A. Chrysochoidis, C.S. Rekatsinas, D.A. Saravanos, A semi-active shunted piezoelectric tuned-mass-damper for multi-modal vibration control of large flexible structures, J. Sound Vib. 537 (2022) 117222, http://dx.doi.org/10.1016/j.jsv.2022.117222, URL https://www.sciencedirect.com/science/article/pii/S0022460X22004114.

[56] Y. Yuan, H. Chen, H. Xu, Y. Jin, G. Chen, W. Zheng, W. Wang, Y. Wang, L. Gao, Highly sensitive and wearable bionic piezoelectric sensor for human respiratory monitoring, Sensors Actuators A 345 (2022) 113818, http://dx.doi.org/10.1016/j.sna.2022.113818, URL https://www.sciencedirect.com/science/article/pii/S0924424722004538.

[57] L. Dong, J. Wang, D. Wang, Modeling and design of three-dimensional voxel printed lattice metamaterials, Addit. Manuf. 69 (2023) 103532, http://dx.doi.org/10.1016/j.addma.2023.103532, URL https://www.sciencedirect.com/science/article/pii/S2214860423001458.

[58] Z. Han, K. Wei, Multi-material topology optimization and additive manufacturing for metamaterials incorporating double negative indexes of Poisson's ratio and thermal expansion, Addit. Manuf. 54 (2022) 102742, http://dx.doi.org/10.1016/j.addma.2022.102742, URL https://www.sciencedirect.com/science/article/pii/S2214860422001464.